MATERIALS PHYSICS AND MECHANICS RESEARCH ARTICLE

Submitted: September 24, 2024 **Revised: February 12, 2025** **Accepted: March 26, 2025**

Modelling forced convection and magneto-elastic interactions in a downward conduit using ferrofluid

H. Derraz ✉, **M. Bouzit**, **A. Bencherif**

Laboratory of Maritime Sciences and Engineering LSIM Faculty of Mechanical Engineering,

University of Science and Technology of Oran, Mohamed Boudiaf, El Mnaouar, Oran, Algeria

✉ hanaa.derraz@univ-usto.dz

ABSTRACT

An unsteady numerical investigation of fluid-structure interaction in forced magnetohydrodynamic convection of a ferrofluid within a downward step configuration, aiming to analyze its influence on flow dynamics and heat transfer mechanisms is presented. The research explicitly incorporates the deformation of an elastic top wall under the combined effects of hydrodynamic, magnetic, and thermal forces. This approach enhances the understanding of the interplay between wall deformation and forced convection under dynamic magnetic fields, an aspect rarely addressed in existing literature. The study examines the impact of key physical parameters, including the Reynolds number ($100 \leqslant Re \leqslant 200$), Hartmann number ($0 \leqslant Ha \leqslant 50$), Cauchy number ($10^{-7} \leqslant Ca \leqslant 10^{-3}$), magnetic field inclination angle ($0° \leqslant \gamma \leqslant 60°$), and nanoparticle volume fraction ($0\ \% \leqslant \varphi \leqslant 8\ \%$) on flow structure, heat transfer, and wall deformation. The numerical modeling is based on the arbitrary Lagrangian-Eulerian formulation, solving the coupled Navier-Stokes, energy, and structural displacement equations using the finite element method. The results reveal that increasing the Reynolds number enhances thermal agitation and vortex formation, leading to improved heat transfer, while a decrease in the Cauchy number amplifies these effects. Conversely, a higher Hartmann number strengthens Lorentz forces, suppressing flow motion and stabilizing the thermal boundary layer. Furthermore, the inclination angle of the magnetic field significantly influences wall deformation, altering the interaction between the ferrofluid and the elastic boundary.

KEYWORDS

forced convection • magnetic fields • elasticity • heat transfer • Hartmann number • MHD • FSI

Citation: Derraz H, Bouzit M, Bencherif A. Modelling forced convection and magneto-elastic interactions in a downward conduit using ferrofluid. *Materials Physics and Mechanics*. 2025;53(2): 83–103.
http://dx.doi.org/10.18149/MPM.5322025_8

Introduction

Convective heat transfer of fluids influenced by magnetic fields and nanoparticles has become an increasingly significant research area within the scientific community. The advent of nanofluids fluids containing nanometer-sized particles suspended in a base fluid has further heightened interest in this field due to their unique thermophysical properties. These nanofluids interact complexly with electromagnetic forces, making them a crucial subject of study for understanding the mechanisms governing fluid behavior under such conditions.

Researchers are actively exploring the wide range of potential benefits that this technology offers across various domains. For instance, in electronics, nanofluids subjected to magnetic fields are employed to cool electronic components, thereby enhancing both their performance and longevity. In the medical field, this technology

facilitates more effective and less invasive targeting and treatment of cancerous tumors. Furthermore, in industrial processes, particularly in heating, ventilation, and air conditioning (HVAC) systems, nanofluids improve energy efficiency, resulting in reduced costs and a smaller environmental footprint for buildings. Precise temperature control enabled by nanofluids also holds promise for more efficient manufacturing processes and higher-quality products.

Recent studies have placed increasing emphasis on the effects of magnetic fields on nanofluids, unveiling new possibilities for enhancing the performance of heat transfer systems in sectors such as microelectronics, cooling systems, industrial processes, and energy and biomedical technologies. These advancements have the potential to revolutionize thermal management in electronic devices, optimize manufacturing processes, and drive the development of innovative medical technologies.

In [1], it was studied forced convective flow within a backward step containing a fixed-diameter rotary cylinder using the ferrofluid Fe_3O_4-H_2O in the presence of an external magnetic field. Their findings demonstrated that while the average Nusselt number decreases as the Hartmann number increases, the nanoparticle concentration and the magnetic field's inclination led to an increase in the average Nusselt number. In [2], it was examined the effects of step height on flow and heat transfer properties, finding that both the average Nusselt number and the skin friction coefficient increase with step height. Several other studies have investigated the effects of nanoparticles on heat transfer in a backward-facing step configuration [3–6]. These studies consistently found that the volume fraction of nanoparticles increases along with the average Nusselt number. In [7], authors used the step length of the backward-facing step as a control parameter in their numerical study and revealed that an increase in step length leads to a higher Nusselt number. In [8], the impact of the ferrofluid Fe_3O_4-H_2O was examined on a backward-facing step in the presence of an inclined magnetic field using a forced convective current. They found that when the cylinder rotates counterclockwise, the rate of heat transfer increases. Additionally, it was studied forced convection ferrofluid flow in a backward-facing step with a pinched cylinder, discovering that adding a fin to the cylinder significantly enhances heat transfer [9]. In [10], it was identified that an oscillating fin mounted on a backward-facing step is the most effective method, as it results in a high average Nusselt number and low-pressure drop. In [11], it was investigated the impact of a baffle on flow and heat transfer distributions in a rectangular duct near a backward-facing step through numerical simulations. Their findings indicate that variations in the Reynolds number and aspect ratio influence heat transfer characteristics and fluid flow properties during separation and reattachment. The influence of the Reynolds number on heat transfer characteristics, showing a significant impact on heat transfer during flow over a backward-facing step, was numerically examined [12]. In [13], a numerical analysis was conducted to investigate the impact of the Reynolds number on the flow characteristics over a BFS. The findings showed that Reynolds number variation affects the diameters of recirculation districts. In [14], it was studied the impact of a baffle mounted on the upper wall of a conduit based on laminar and turbulent mixed convection. The results indicate that baffle height, position, and distance all have a significant impact on the properties of heat transfer and fluid flow.

Numerical studies have extensively explored the effects of adding nanoparticles to a base fluid on heat transfer performance. Research by [15–19] demonstrated that the incorporation of nanoparticles increases the average Nusselt number, enhances mass transfer, and improves flow characteristics as the volume fraction of nanoparticles rises [20]. Experiments were conducted comparing two nanofluids, CuO-EG and MgO-EG, and it was found that the CuO-EG nanofluid exhibited a higher heat transfer rate than the MgO-EG nanofluid. Similarly, through numerical simulations of mixed convection in laminar nanofluids, revealed that both the shape and type of nanoparticles significantly influence flow properties, with nanofluids generally providing superior heat transfer compared to water alone [21]. In [22], it was investigated the magnetohydrodynamic (MHD) boundary layer flow of three types of nanofluids, focusing on heat and mass transfer in porous media. More recently, it was examined the impact of magnetic nanoparticles on the thermophysical properties of nanofluids and forced convective heat transfer, concluding that increasing the magnetic field (MF) and nanoparticle (NP) concentrations leads to a corresponding increase in the Nusselt number of the nanofluids [23].

Several studies have examined the fluid flow characteristics and heat transfer quality in systems involving a rotating cylinder. In [24–26], it was found that high Reynolds number values significantly increase the average Nusselt number, and that flow instability positively impacts forced convection heat transfer, particularly on the cylinder's surface. Further, it was investigated ferrofluid flow-induced convection over a descending step using a spinning finned cylinder [27]. Their study revealed that the rotation of the finned cylinder enhanced heat transfer by 177.33 % compared to a cylinder without a fin.

Additionally, the influence of external magnetic fields on thermal transfer control and quality in systems with an inclined and rotated cylinder has been extensively studied by [28–30]. These studies concluded that an inclined magnetic field effectively eliminates recirculation zones, and that a higher Reynolds number further enhances heat transfer.

Numerous studies have investigated the impact of nanofluids on thermal and hydrodynamic properties in enclosures using magneto-hydrodynamic (MHD) forced convection. Research by [31–35] has shown that the temperature gradient increases with the Hartmann number, and the Nusselt number's growth is influenced by domain velocity and permeability. These studies also found that magnetic forces improve conduction, and the inclusion of nanofluids enhances overall heat transfer. Additionally, it was observed that the lowest wall of the cavity is sensitive to the elastic wall, while the top wall shows an increase in temperature gradient with the Hartmann number.

Further investigations into the forced convection of non-Newtonian nanofluids in wavy channels [36,37] revealed that the addition of nanoparticles and an increase in the Reynolds number significantly enhance heat transfer in such channels. In [38], it was studied magnetohydrodynamic mixed convection in a 3D lid-driven enclosure containing a Cu-water nanofluid, while in [39] it was focused on steady MHD mixed convective cooling in a vented, porous cavity with an intense elliptical inward cylinder containing MWCNT/CMC nanofluid. Their results demonstrated that Nusselt numbers increase with Richardson number and porosity ratio, although the Hartmann number tends to dominate at lower levels of fluidity within the cavity. Finally, it was investigated transient mixed convection in a vented square container with heated walls and a flexible baffle, finding

that the enhanced average Nusselt number is most prominent in cavities with flexible baffles [40]. The effect of a flexible fin on unsteady natural convection of a Bingham fluid in a laterally heated square cavity is analyzed in [41]. The results indicate that heat transfer reaches its peak at $Ra = 10^5$ when $Bn = 0$, while an increasing Bingham number gradually suppresses convection, ultimately leading to a conduction-dominated regime at $Bn = 20$. In contrast, the modulus of elasticity of the fin has a negligible impact on heat transfer.

In the present study, the coupling effects of forced magnetic field convection and elastic membrane deformation in a descending ferrofluid conduit. This work analyzed various levels of Reynolds number, elasticity, Hartmann number, and magnetic field tilt angle and nanoparticle volume fraction.

Modeling approach

A two-dimensional unsteady numerical study has been carried out to examine the flow of a nanofluid subjected to forced convection in the presence of an external magnetic field. This study focuses on a one-step backward-facing configuration with an elastic top wall incorporating a non-rotating cylinder. Figure 1 illustrates the physical configuration and associated boundary conditions. The length of the rearward-facing step is denoted H, and the height of the horizontal duct is $2H$. The cylinder has a radius of $D = H$, with a central position at ($4H$, H). At the entrance to the duct, the velocity is $u = u_0$ and $v = 0$. At the outlet of the pipe, all the gradients of the variables in the x direction are zero. The associated temperatures are T_c for the low temperature of the ferrofluid and Th for the high temperature of the bottom wall. The Prandtl number of the base fluid is maintained at 6.2, and the constant thermophysical properties of H_2O and Fe_3O_4 are listed in Table 1.

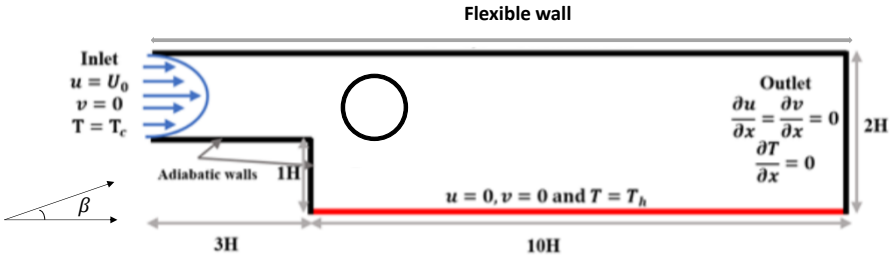

Fig. 1. Physical model

Table 1. Thermo-physical properties of Water and Iron Oxide

Thermophysical properties	ρ, kg/m^3	Cp, J/kg·K)	k, W/m·K	β, 1/K	σ, 1/Ω·m
Water	997.1	4,179	0.613	$21 \cdot 10^{-5}$	0.05
Fe_3O_4	5,200	670	6	$1.18 \cdot 10^{-5}$	25,000

Hence, the thermophysical properties were considered independent of temperature. Employing the assumptions revealed earlier and using the Arbitrary Lagrangian-Eulerian (ALE) method, the equations modelling the hydrodynamic and thermal characteristics of the problem are presented as follows [8,41].

For fluid domain:

$$\frac{\partial u}{\partial x}+\frac{\partial v}{\partial y}=0. \tag{1}$$

Momentum equations:

$$\rho_{nf}\left[\frac{\partial u}{\partial t}+u\frac{\partial u}{\partial x}+v\frac{\partial u}{\partial y}\right]=-\frac{\partial p}{\partial x}+\mu_{nf}\left[\frac{\partial^2 u}{\partial x^2}+\frac{\partial^2 u}{\partial y^2}\right]+\sigma_{nf}B_0\left(v\sin\gamma\cos\gamma-u\sin^2\gamma\right); \tag{2}$$

$$\rho_{nf}\left[\frac{\partial v}{\partial t}+u\frac{\partial v}{\partial x}+v\frac{\partial v}{\partial y}\right]=-\frac{\partial p}{\partial y}+\mu_{nf}\left[\frac{\partial^2 v}{\partial x^2}+\frac{\partial^2 v}{\partial y^2}\right]+\sigma_{nf}B_0\left(u\sin\gamma\cos\gamma-v\sin^2\gamma\right). \tag{3}$$

The energy equation for the fluid:

$$\frac{\partial T}{\partial t}+u\frac{\partial T}{\partial x}+v\frac{\partial T}{\partial y}=\alpha_{nf}\left(\frac{\partial^2 T}{\partial x^2}+\frac{\partial^2 T}{\partial y^2}\right). \tag{4}$$

For elastic structure domain, the equations of the motion of flexible fins can be written as:

$$\rho_s\frac{\partial^2 d_x}{\partial t^2}-\frac{\partial \sigma^*_{xx}}{\partial x}-\frac{\partial \sigma^*_{xy}}{\partial y}=0; \tag{5}$$

$$\rho_s\frac{\partial^2 d_y}{\partial t^2}-\frac{\partial \sigma^*_{xy}}{\partial x}-\frac{\partial \sigma^*_{yy}}{\partial y}=0. \tag{6}$$

The energy equation for the flexible fin:

$$\rho_s c_{ps}\frac{\partial^2 T_s}{\partial t^2}=k_s\left(\frac{\partial^2 T_s}{\partial x^2}-\frac{\partial^2 T_s}{\partial y^2}\right). \tag{7}$$

The Neo-Hookean solid model is applied to express the stress tensor of Eqs. (5) and (6). The tensor σ is given by:

$$\boldsymbol{\sigma}^*=J^{-1}FSF^{tr}\,\Big|F=(I+\nabla^*\mathbf{d}_s^*),J=\det(F)\;\&\;S=\partial W_s/\partial\varepsilon; \tag{8}$$

$$W_s=\frac{1}{2}l(J^{-1}I_1-3)-lLn(J)+\frac{1}{2}\lambda(Ln(J))^2;$$

$$\begin{vmatrix} l=E/(2(1+\nu)) \\ \lambda=E\nu/((1+\nu)(1-2\nu)) \end{vmatrix}; \tag{9}$$

$$\varepsilon=\frac{1}{2}\left(\nabla^*\mathbf{d}_s^*+\nabla^*\mathbf{d}_s^{*tr}+\nabla^*\mathbf{d}_s^{*tr}\nabla^*\mathbf{d}_s^*\right). \tag{10}$$

The boundary conditions pertinent to the external walls and the interface of the flexible upper wall can be formulated as follows:

1. the inlet: $u=u_0$, $v=0$, $T=T_c$;
2. the downstream bottom wall: $u=0$, $v=0$, $T=T_h$;
3. the outlet: $\frac{\partial u}{\partial n}=\frac{\partial T}{\partial n}=0$;
4. other walls are adiabatic and the velocity is no-slip: $u=v=0$ and $\partial T/\partial n=0$;
5. the adiabatic cylinder: $\partial T/\partial n=0$;
6. the cylinder velocity components: $u=v=0$.

The dimensionless form equations: $X=\frac{x}{H}$, $Y=\frac{y}{H}$, $\theta=\frac{T-T_c}{T_h-T_c}$, $P_r=\frac{\nu_f}{\alpha_f}$, $\mathrm{Ha}=B_0H\sqrt{\frac{\sigma_{nf}}{\mu_{nf}}}$, $\mathrm{Re}=\frac{H\tilde{u}}{\nu_f}$, $\tau=\frac{t\alpha}{H^2}$, $\sigma^*=\frac{\sigma}{E}$, $P=\frac{p}{\rho_{nf}\tilde{u}^2}$, $U=\frac{u}{\tilde{u}}$, $V=\frac{v}{\tilde{u}}$.

The governing dimensionless equations are hence. Mass balance:

$$\frac{\partial U}{\partial X}+\frac{\partial V}{\partial Y}=0. \tag{11}$$

Momentum balance:

$$\frac{\partial U}{\partial \tau}+U\frac{\partial U}{\partial X}+V\frac{\partial U}{\partial Y}=-\frac{\partial P}{\partial X}+\frac{1}{\mathrm{Re}}\frac{\rho_f}{\rho_{nf}}\frac{\mu_{nf}}{\mu_{nf}}\left(\frac{\partial^2 U}{\partial X^2}+\frac{\partial^2 U}{\partial Y^2}\right)+\frac{\rho_f}{\rho_{nf}}\frac{\sigma_{nf}}{\sigma_f}\frac{\mathrm{Ha}^2}{\mathrm{Re}}\left(V\sin\gamma\cos\gamma-U\sin^2\gamma\right); \tag{12}$$

$$\frac{\partial V}{\partial \tau}+U\frac{\partial V}{\partial X}+V\frac{\partial V}{\partial Y}=-\frac{\partial P}{\partial Y}+\frac{1}{\mathrm{Re}}\frac{\rho_f}{\rho_{nf}}\frac{\mu_{nf}}{\mu_{nf}}\left(\frac{\partial^2 V}{\partial X^2}+\frac{\partial^2 V}{\partial Y^2}\right)+\frac{\rho_f}{\rho_{nf}}\frac{\sigma_{nf}}{\sigma_f}\frac{\mathrm{Ha}^2}{\mathrm{Re}}\left(U\sin\gamma\cos\gamma-V\sin^2\gamma\right). \tag{13}$$

The energy equation for the fluid:

$$\frac{\partial \theta_f}{\partial \tau}+U\frac{\partial \theta_f}{\partial X}+V\frac{\partial \theta_f}{\partial Y}=\frac{1}{\mathrm{Re}\times\mathrm{Pr}}\frac{\alpha_{nf}}{\alpha_f}\left(\frac{\partial^2 \theta_f}{\partial X^2}+\frac{\partial^2 \theta_f}{\partial Y^2}\right). \tag{14}$$

Structural displacement of the flexible fin:

$$\frac{\rho_s}{\mathrm{Ca}}\frac{\partial^2 D_X}{\partial \tau^2}-\frac{\partial \Gamma_{XX}}{\partial X}-\frac{\partial \Gamma_{XY}}{\partial Y}=0; \tag{15}$$

$$\frac{\rho_s}{\mathrm{Ca}}\frac{\partial^2 D_Y}{\partial \tau^2}-\frac{\partial \Gamma_{XY}}{\partial X}-\frac{\partial \Gamma_{YY}}{\partial Y}=0. \tag{16}$$

The energy equation for the fin:

$$\frac{\partial^2 \theta_s}{\partial \tau^2}=k_s\left(\frac{\partial^2 \theta_s}{\partial X^2}-\frac{\partial^2 \theta_s}{\partial Y^2}\right). \tag{17}$$

Nusselt number:

$$\mathrm{Nu}=\frac{\kappa_{nt}}{\kappa_{nf}}\left(\frac{\partial \theta}{\partial Y}\right). \tag{18}$$

The average Nusselt number:

$$\mathrm{Nu}_{avg}=\frac{1}{L}\int_0^L \mathrm{Nu}dX. \tag{19}$$

Thermo-physical properties of ferrofluid are presented below.

Density:

$$\rho_{nf}=(1-\phi)\rho_f+\phi\rho_p. \tag{20}$$

Thermal diffusivity:

$$\alpha_{nf}=\frac{k_{nf}}{(\rho c_p)_{nf}}. \tag{21}$$

Electrical conductivity:

$$\delta_{nf}=\delta_f\left[1+\frac{3(\delta-1)\phi}{(\delta+2)-(\delta-1)\phi}\right];\ \delta=\frac{\delta_p}{\delta_f}. \tag{22}$$

Specific heat:

$$(\rho c_p)_{nf}=(1-\phi)(\rho c_p)_f+\phi(\rho c_p)_p. \tag{23}$$

Thermal expansion coefficient:

$$(\rho\beta)_{nf}=(1-\phi)(\rho\beta)_f+\phi(\rho\beta)_p. \tag{24}$$

Thermal conductivity:

$$\frac{k_{nf}}{k_f} = \frac{k_p + 2k_f - 2\phi(k_f - k_p)}{k_p + 2k_f + \phi(k_f - k_p)}. \quad (25)$$

Dynamic viscosity:

$$\mu_{nf} = \frac{\mu_f}{(1-\phi)^{2.5}}. \quad (26)$$

Dimensionless Boundary conditions:

1. the inlet: $U = U_0$, $V = 0$; $\theta = 0$;
2. the downstream bottom wall: $U = 0$, $V = 0$, $\theta = 1$;
3. the outlet: $\partial U/\partial X = \partial V/\partial Y = 0$, $\partial\theta/\partial X = 0$;
4. Other walls are adiabatic and the velocity is no-slip: $U = V = \partial\theta/\partial n = 0$;
5. the adiabatic cylinder: $\partial\theta/\partial n = 0$;
6. the cylinder velocity components: $U = V = 0$.

Numerical solution method: Grid independency test and Validation

Numerical solution method

Numerical methods are utilized to tackle the governing equations and boundary conditions for unsteady Forced convection of a magneto-elastic interactions in a downward conduit using ferrofluid. The equations are first reformulated for simplicity, then solved using the Galerkin Method of Weighted Residuals, a variant of the Finite Element Method (FEM). The fluid-structure interface, including the dynamic motion of the flexible wall, is captured using the Arbitrary Lagrangian-Eulerian (ALE) method. The computational domain is finely discretized into non-uniform triangular elements, ensuring precise flow field representation. To address the nonlinear momentum equations, a Newton iteration algorithm is applied.

Grid independency test

To validate that the results obtained are not influenced by the size of the mesh used, a mesh independence test was carried out. This test consists of analysing the evolution of the average Nusselt number as a function of dimensionless time on the hot wall for different levels of mesh refinement. The parameters used are *Re* = 150; *Ha* = 25, *Ca* = 10^{-4}, γ = 0° and φ = 5 %. The results are shown in Table 2, where it can be seen that variations in the average Nusselt number as a function of time become negligible from a mesh size greater than 80283. Consequently, this mesh size (Fig. 2) was chosen to present the results in the rest of the study.

Table 2. Grid independence test at Re = 150; Ha = 25, Ca = 10^{-4}, γ = 0° and φ = 5 %

Elements Number	19846	27721	42512	**80283**	136134
Time	2640 s	4830 s	7167 s	**14820 s**	17635 s
Nu_{avg}	4.680953	4.669642	4.667470	**4.667216**	4.667101

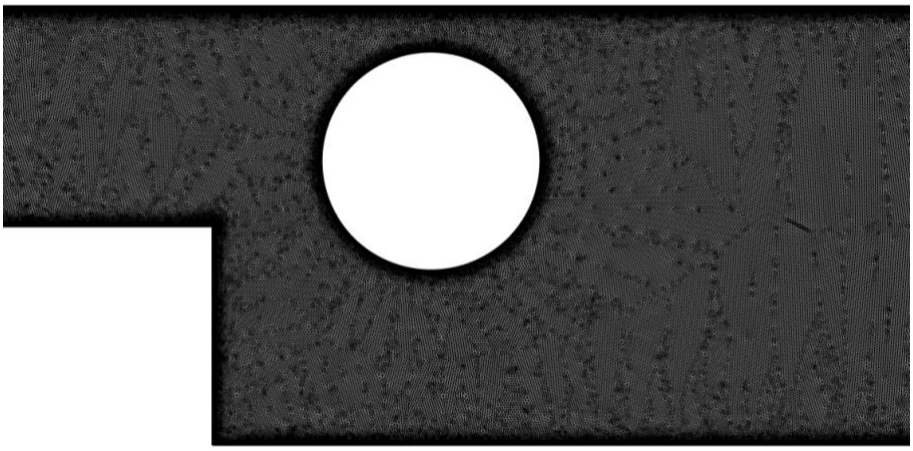

Fig. 2. The physical configuration with the best mesh size

Validation

To further validate the calculation code used in this study, we compared our results with the numerical data reported by [8] for the case of forced convection over a downward step, with *Re* set at 100 and *Pr* at 5. Figure 3 illustrates this comparison, demonstrating good agreement between the two sets of results. Further validation was conducted by comparing the mean Nusselt number as a function of the Hartmann number (*Ha*) reported by [8] with the results obtained in the present work.

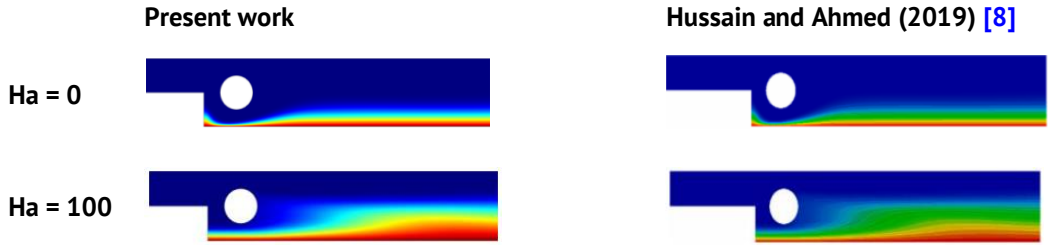

Fig. 3. Comparing the results of the present study and reported by [8]

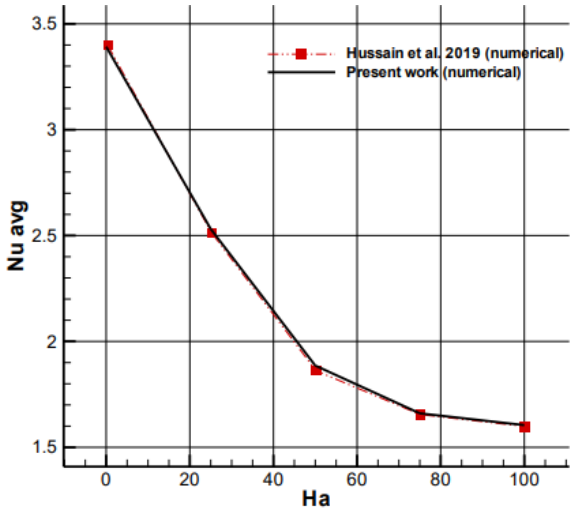

Fig. 4. Comparing the results of the present study and Nusselt number reported by [8]

As shown in Fig. 4, excellent agreement is observed between the present study and the previously reported data. These comparisons bolster the accuracy and reliability of the calculation code used in this research, demonstrating its effectiveness in simulating and predicting the complex interactions and phenomena within the system. The alignment between the results reinforces confidence in the underlying mathematical models and numerical methods employed in the code.

Results and Discussion

This section delves into the analysis of how changing key control parameters, specifically the dimensionless Reynolds $100 \leqslant Re \leqslant 200$, Hartmann $0 \leqslant Ha \leqslant 50$, and Cauchy$10^{-7} \leqslant Ca \leqslant 10^{-3}$ numbers, nanoparticles concentration $0\ \% \leqslant \varphi \leqslant 8\ \%$, magnetic field inclination $0° \leqslant \gamma \leqslant 60°$, affects various aspects. We explore how these parameters shape flow characteristics, like streamlines, and thermal fields, as indicated by isotherm contours. Moreover, we meticulously investigate the consequences of these parameter shifts on overall heat transfer performance and structural deformation. This examination involves scrutinizing curves that chart the progression of both the mean Nusselt number, local Nusselt number and the displacement field.

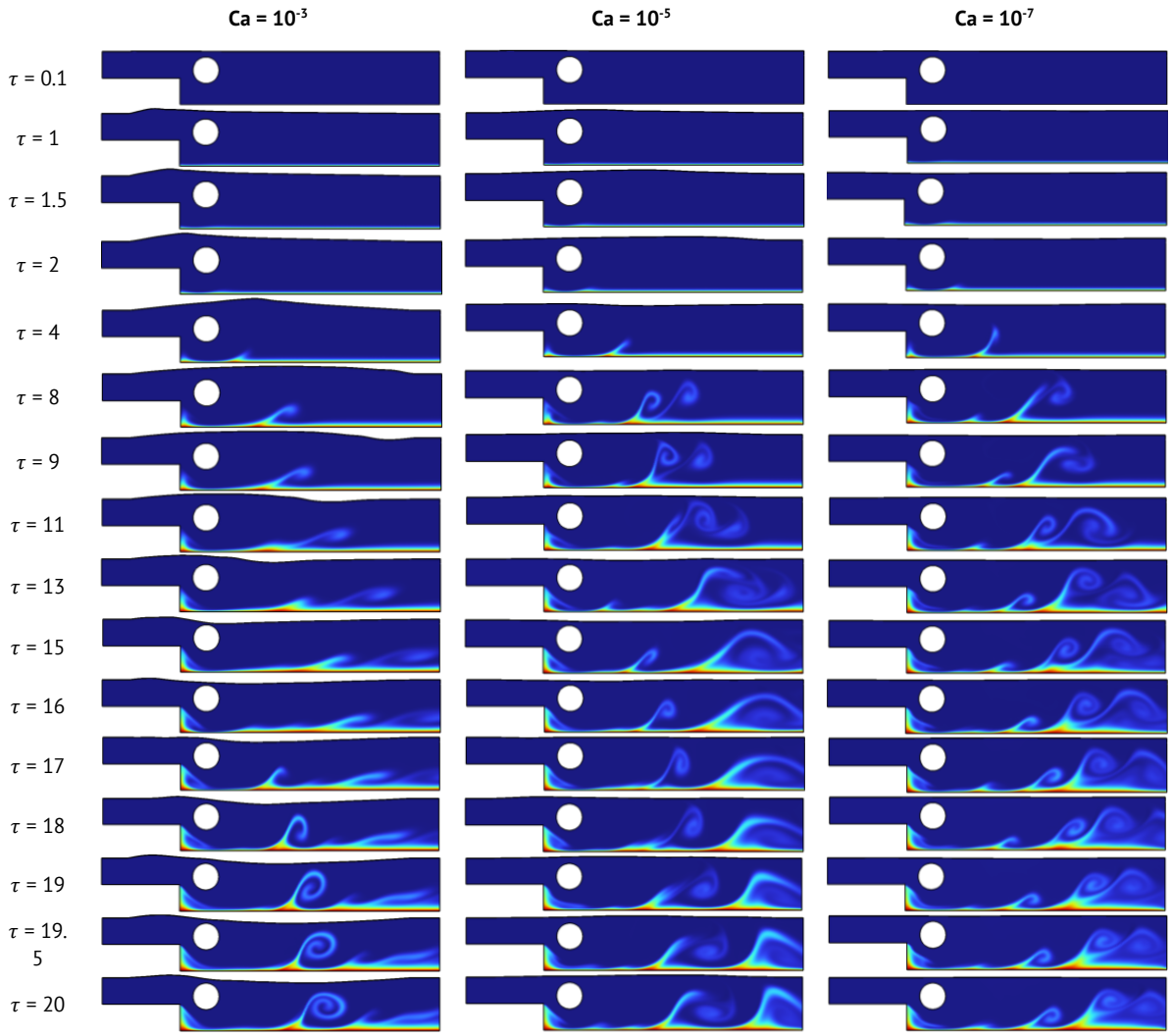

Fig. 5. Development of isotherms with time for $Re = 150$, $Ha = 0$, $\gamma = 0°$ at $\varphi = 5\ \%$

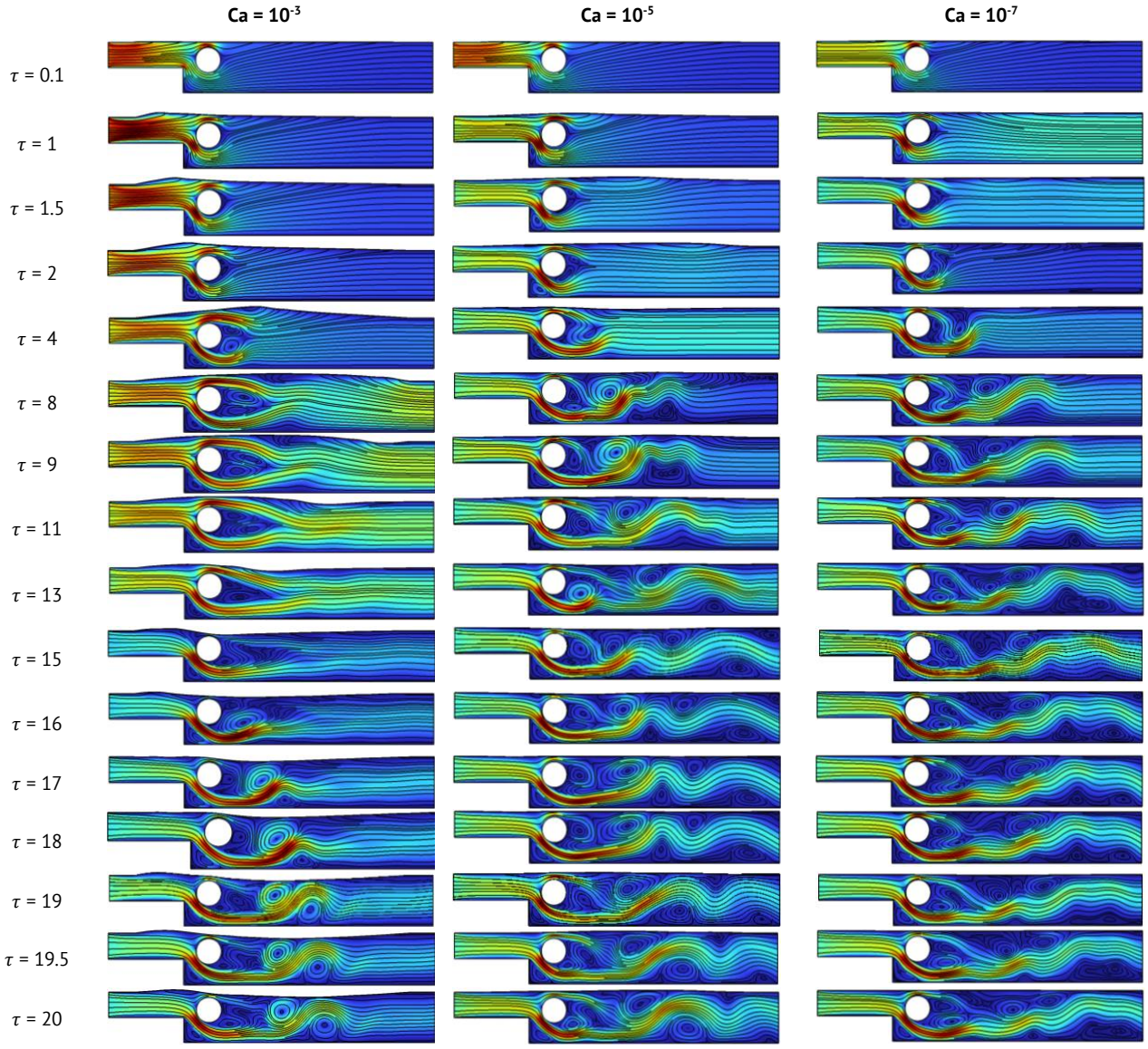

Fig. 6. Development of streamlines with time for *Re* = 150, *Ha* = 0, γ = 0° and φ = 5 %

Figures 5 and 6 illustrate the variation of isotherms and streamlines as a function of time for distinct values of the Cauchy number, with *Re* set at 150, *Ha* = 0, γ = 0°, φ = 5% and *Pr* at 6.2. During the initial phases (beginning from τ = 0 to 2), the analysis of isotherms unveiled an initial deformation of the elastic top wall, a phenomenon that exhibits a proportional decrease in response to the reduction in the Cauchy number. Concurrently, the streamlines indicated a notable acceleration of flow at the channel entrance, followed by a gradual attenuation as the Cauchy number diminished. These observations can be attributed to variations in viscosity and temperature distribution induced by changes in the Cauchy number. In the subsequent time interval (extending from τ = 4 to 11), a substantial increase in the perturbation of the thermal boundary layer was observed. This disturbance exhibited an amplifying trend in tandem with the decrease in the Cauchy number, resulting in enhanced wall stiffening. Simultaneously, an increase in the deformation of the upper wall was recorded, presenting an inverse proportional relationship with the Cauchy number. These observations collectively suggest a significant correlation between fluid

thermodynamics, wall deformation, and the Cauchy number, underscoring the importance of Multiphysics interactions in this experimental setup. During this same period, the streamlines revealed an increasing formation of vortices downstream of the channel, specifically behind the cylinder. This rise in vortex occurrence appears intrinsically linked to the decrease in the Cauchy number, emphasizing the major influence of this parameter on flow dynamics. In the subsequent time range (commencing from $\tau = 13$ to 16), a significant intensification was observed in both vortex formation and thermal boundary layer perturbation. Notably, a distinct deviation of the elastic upper wall was detected specifically for Cauchy $Ca = 10^{-3}$. This deviation can be attributed to complex forces resulting from magnetohydrodynamic interactions and thermal variations induced by the magnetic field and the Cauchy number. Finally, from $\tau = 17$ onwards, stability emerged in both the isotherms and streamlines, suggesting that the system has reached a state of equilibrium or is converging towards a steady-state. These comprehensive observations highlight the richness of physical phenomena involving fluid-thermal-magnetic interactions and emphasize the need for a profound understanding of the parameters for a complete interpretation of the system's dynamic behavior.

Figures 7 and 8 show the isotherms and streamline contours for various Reynolds and Cauchy numbers, with $Ha = 0$, $Pr = 10$, $\varphi = 5$ % and $\gamma = 0°$. As shown in the figures, an increase in the Reynolds number leads to significant agitation within the thermal boundary layer, along with a rise in the number of vortices. Conversely, a decrease in the Cauchy number results in increased disturbance in the thermal boundary layer and a corresponding increase in vortex formation. The relationship between the Reynolds number and the dominance of velocity-related inertial forces over viscous forces is apparent. This dominance leads to faster flow and, consequently, enhanced heat transfer rates. Furthermore, the intensification of vortices with increasing Reynolds number contributes to the augmentation of forced convection within the thermal boundary layer.

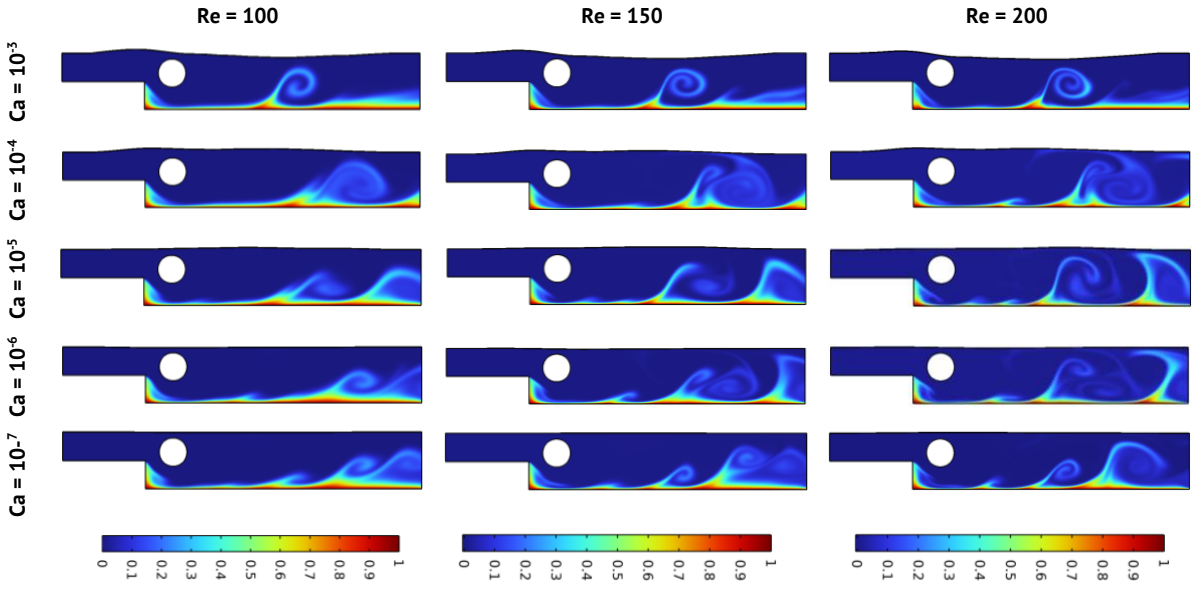

Fig. 7. Effect of Reynolds number *Re* with different values of Cauchy number one isotherms with $Ha = 0$, $Pr = 6.2$, $\varphi = 5$ % and $\gamma = 0°$

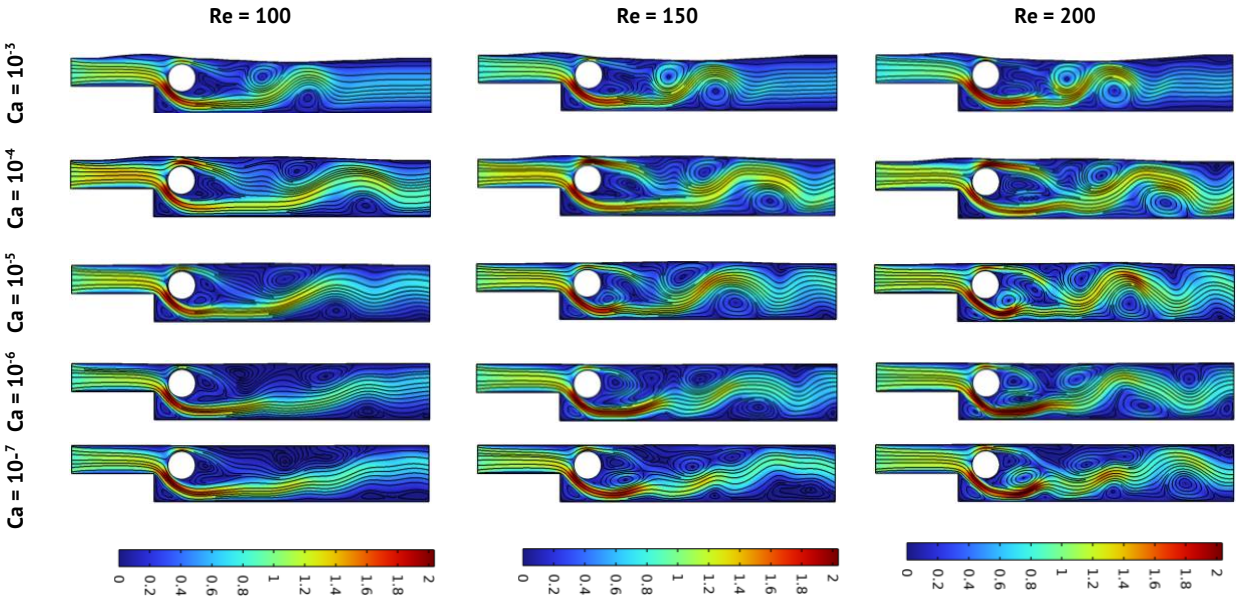

Fig. 8. Effect of Reynolds number *Re* with different values of Cauchy number one Streamlines with *Ha* = 0, *Pr* = 6.2, φ = 5 % and γ = 0°

Figure 9 illustrates the variation of the average Nusselt number as a function of *Ha* for different values of Reynolds number and Cauchy number, with *Pr* = 6.2, φ = 5 % and γ = 0°. It should be noted that increasing the Reynolds number has a favorable impact on improving the average Nusselt number, as does decreasing the Cauchy number. The increase in Reynolds number results in an intensification of the inertial forces associated with velocity, leading to an acceleration of fluid motion. Consequently, it can be concluded that, as the Reynolds number increases, heat transfer improves, manifested by an increase in the Nusselt number.

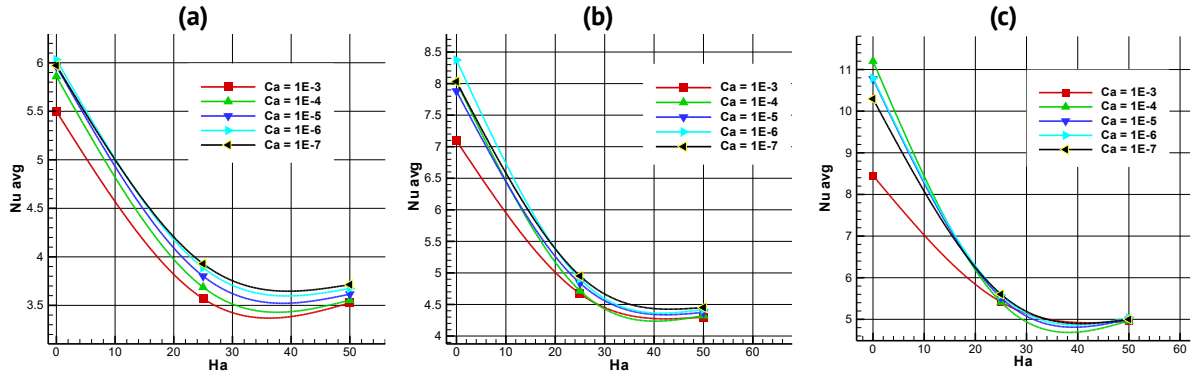

Fig. 9. Effect of Reynolds number *Re* with different values of Cauchy number one average Nusselt number with *Pr* = 6.2, φ = 5 % and γ = 0°: (a) *Re* = 100; (b) *Re* = 150, (c) *Re* = 200

Figure 10 presents the variation of local Nusselt number with Reynolds number along the hot wall for γ = 0°, φ = 5 %, *Ca* = 10^{-4} and *Ha* = 25. By observing the graphs, it is noted that the increase in Reynolds number leads to an increase in the local Nusselt number. The distribution of the local Nusselt number is maximum near the area between *X* = 3 and *X* = 5, close to the adiabatic cylinder. Moving away from this area, that is, towards *X* = 5 and

beyond, the Nusselt number starts to gradually decrease towards the outlet. This distribution is due to the increase in Reynolds number, and thus the inertial forces relative to the viscous forces favor convection phenomena, which are particularly intense in this region where the temperature gradients are most significant. This results in an increase in the local Nusselt number, especially near the adiabatic cylinder.

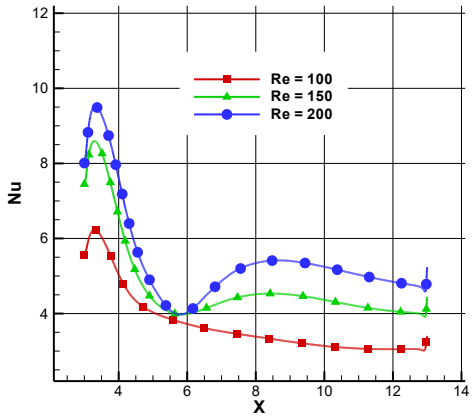

Fig. 10. Effect of Reynolds number on local Nusselt number along the heated wall for γ = 0°, *Ha* = 25, *Ca* = 10^{-4} and φ = 5 %

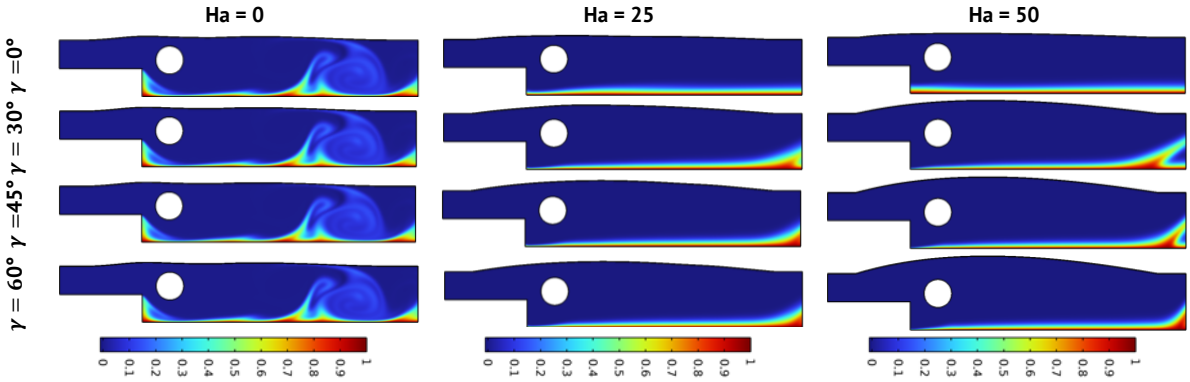

Fig. 11. Effect of Hartmann number *Ha* with different values of angle of magnetic field inclination one isotherms at *Re* = 150, φ = 5 %, *Ca* = 10^{-4} and *Pr* = 6.2

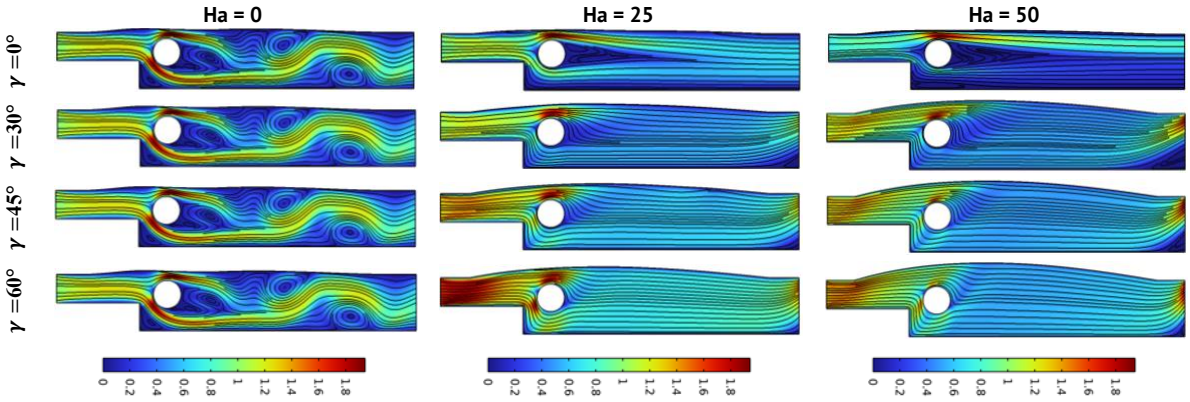

Fig. 12. Effect of Hartmann number Ha with different values of angle of magnetic field inclination one Streamlines at *Re* = 150, φ = 5 %, *Ca* = 10^{-4} and *Pr* = 6.2

Figures 11 and 12 illustrate the effect of varying the angle of magnetic field inclination on the configuration of isotherms and streamlines for different values of Hartmann number at Re = 150, φ = 5 %, Ca = 10^{-4} and Pr = 6.2. As mentioned previously, an increase in the Hartmann number leads to a reinforcement of the Lorentz forces, resulting in a slowing down of the fluid motion and increased thermal boundary layer stabilisation near the heated bottom wall.

Concerning the angle of inclination of the magnetic field, variations in this angle had a significant effect on the increase in deformation of the elastic upper wall, with a maximum deformation noted for γ = 60° and Ha = 50. For the isotherms, an increase in the thickness of the thermal boundary layer is observed as the angle of inclination increases. Regarding the streamlines, an acceleration of the flow at channel entry is noted as the γ number increases.

These behaviours can be explained by the positive impact of the inclination of the magnetic field on the enhancement of forced convection, leading to a gain in heat transfer rate and an overall improvement in the process.

Figure 13 illustrates the impact of varying the angle of magnetic field inclination on the average Nusselt number as a function of the Hartmann number, under specific conditions Re set at 150, Ca at 10^{-4}, Pr at 10, and at φ = 5 %. Upon analyzing the average Nusselt curves, a progressive improvement in this parameter is evident as the angle of inclination increases, signifying an enhancement in heat transfer efficiency. This improvement can be attributed to the favorable influence of the inclination angle on the promotion of convective heat transfer within the fluid domain. The inclined magnetic field disrupts stagnant fluid regions, enhancing the overall heat transfer process and resulting in the observed increase in the average Nusselt number.

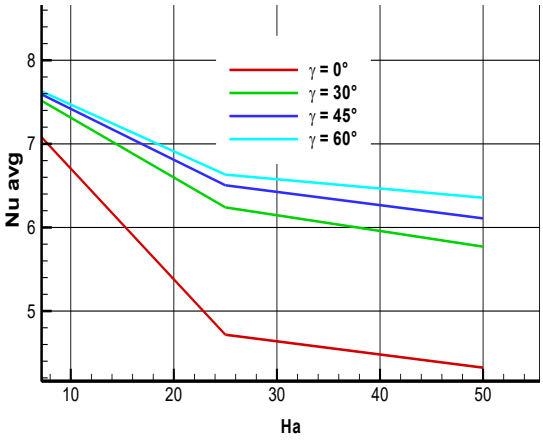

Fig. 13. Effect of Hartmann number Ha with different values of angle of magnetic field inclination one average Nusselt number for Re = 150, Ha = 25, Ca = 10^{-4} and φ = 5 %

Figure 14 illustrates the impact of a growing magnetic field (reflected by the increasing Hartmann number) on heat transfers at the hot wall for a flow characterized by a Reynolds number of 150. A clear trend of decreasing local Nusselt number is observed. This evolution is attributable to the intensification of Lorentz forces, which act as a resistive force opposing the fluid's motion. This braking action induces a reduction in velocity and temperature fluctuations within the fluid, resulting in a stabilized thermal

boundary layer. A more stable thermal boundary layer is less conducive to intense heat exchanges, hence the decrease in the local Nusselt number.

Figure 15 shows the evolution of the local thermal transfer coefficient (Nusselt number) along the hot wall for a flow characterized by a Reynolds number of 150 and a Hartmann number of 25, depending on the inclination of the magnetic field. We observe an increasing trend in the local Nusselt number as the inclination angle of the magnetic field increases. This increase can be explained by the fact that a greater inclination of the magnetic field intensifies the Lorentz forces induced in the fluid, stimulating fluid movements and enhancing heat exchanges at the wall.

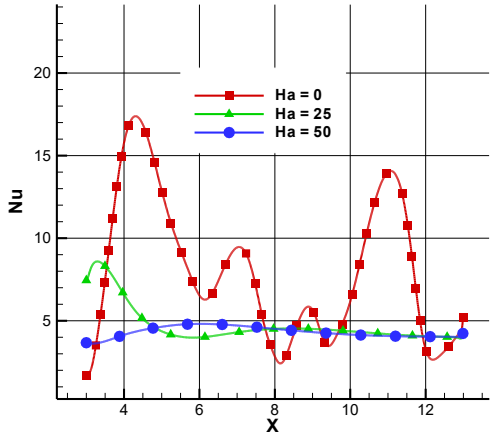

Fig. 14. Effect of Hartmann number on local Nusselt number along the heated wall for Re = 150, Ha = 25, Ca = 10^{-4} and φ = 5 %

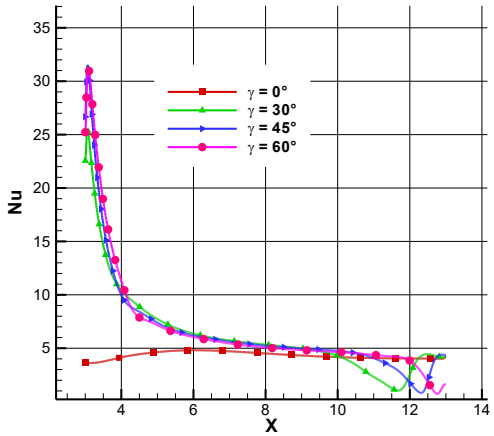

Fig. 15. Effect of magnetic field inclination on local Nusselt number along the heated wall for Re = 150, Ha = 25, Ca = 10^{-4} and φ = 5 %

Figures 16 and 17 demonstrate the influence of varying the concentration of nanoparticles of Fe_3O_4 on the flow configuration as a function of the Hartmann number, for given parameters such as Re = 150, Ca = 10^{-4}, Pr = 6.2 and γ = 0°. The observation shows that the variation in the Hartmann number has a significant influence on the configuration of the isotherms and streamlines compared with the variation in the concentration of the ferrofluid.

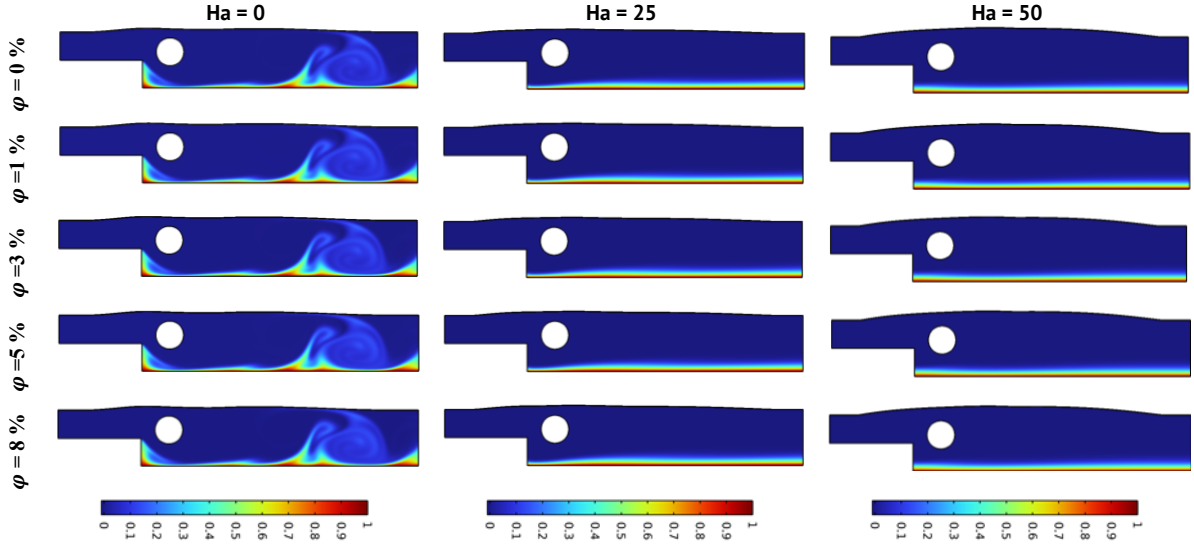

Fig. 16. Effect of nanoparticles concentration φ with different values of Hartmann number at Re = 150, Ca = 10^{-4}, Pr = 6.2 and γ = 0°

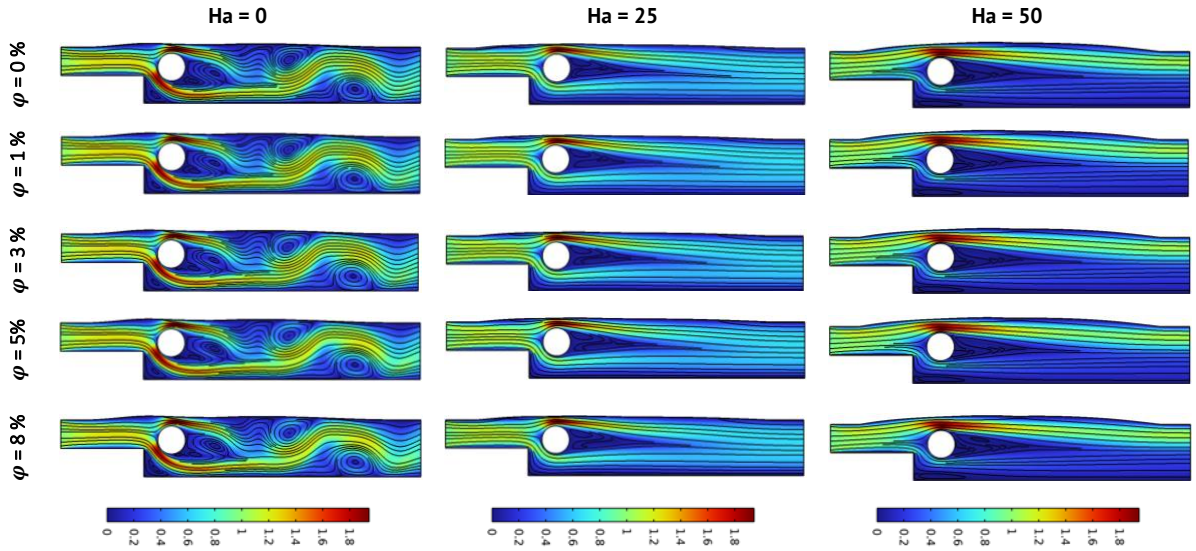

Fig. 17. Effect of nanoparticles concentration φ with different values of Hartmann number at Re = 150, Ca = 10^{-4}, Pr = 6.2 and γ = 0°

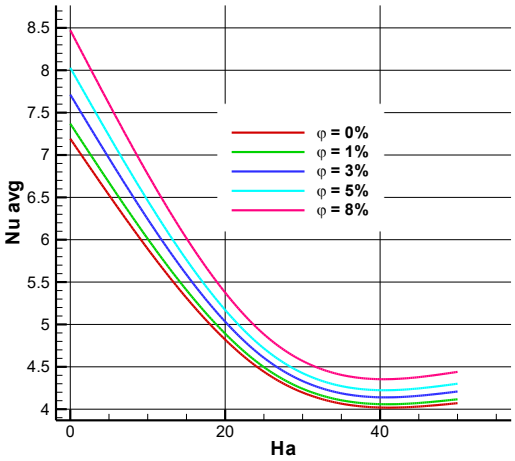

Fig. 18. Effect of ferrofluid concentrations on average Nusselt number along the heated wall for Re = 150, Ha = 25, Ca = 10^{-4} and γ = 0°

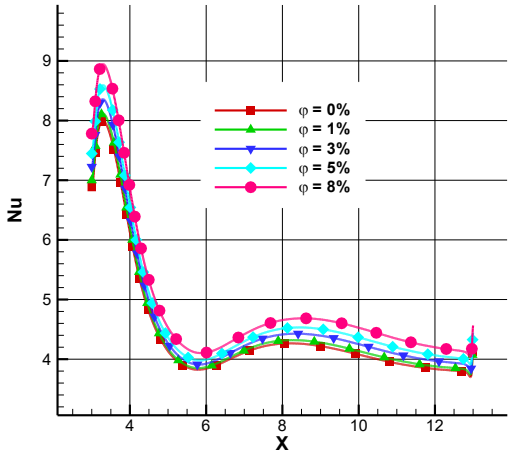

Fig. 19. Effect of ferrofluid concentrations on local Nusselt number along the heated wall for Re = 150, Ha = 25, Ca = 10^{-4} and γ = 0°

Figure 18 shows the variation of the average Nusselt number as a function of Hartmann number for different ferrofluid concentrations, with defined parameters such as Re = 150, Ca = 10^{-4}, Pr = 6.2, and γ = 0°. Examining the average Nusselt curves, it is observed that increasing the ferrofluid concentration has a positive effect on the improvement of the average Nusselt number. This can be attributed to the increase in conductive heat transfer, because incorporating nanoparticles into a base fluid increases the thermal conductivity of the fluid, leading to an improvement in heat transfer compared to the pure fluid.

Figure 19 displays the evolution of the local thermal transfer coefficient along the hot wall for a flow characterized by a Reynolds number of 150, γ=0°, Ca = 10^{-4} and a Hartmann number of 25, depending on the nanoparticle concentration. A positive correlation is observed between the nanoparticle concentration and the local Nusselt

number. Increasing the nanoparticle concentration enhances the fluid's effective thermal conductivity, resulting in an increased local thermal transfer coefficient.

Figure 20 shows the variation in elastic top wall deformation as a function of Cauchy number, for different Reynolds number values at $Ha = 0$, $\varphi = 5$ %, $\gamma = 0°$ and $Pr = 6.2$. The observations reveal an inverse relationship between the deformation of the elastic top wall and the two parameters considered. An increase in Reynolds number is associated with an increase in deformation, suggesting enhanced forced convection and flow acceleration. On the other hand, a decrease in Cauchy number leads to a reduction in deformation, which can be attributed to the increase in wall resistance to deformation resulting from the decrease in this parameter.

Figure 21 shows the impact of varying the Hartmann number (*Ha*) on the deformation of the elastic top wall, for different values of the Cauchy number at $Re = 150$, $\gamma = 0°$, $\varphi = 5$ % and $Pr = 6.2$. It should be noted that the rise in magnetic force, reflected by the increase in Ha number, exerts a favorable influence on the increase in deformation. Corresponding to previous observations, the reduction in the Cauchy number indicates a strengthening of the wall's resistance to deformation, resulting in a reduction in said deformation.

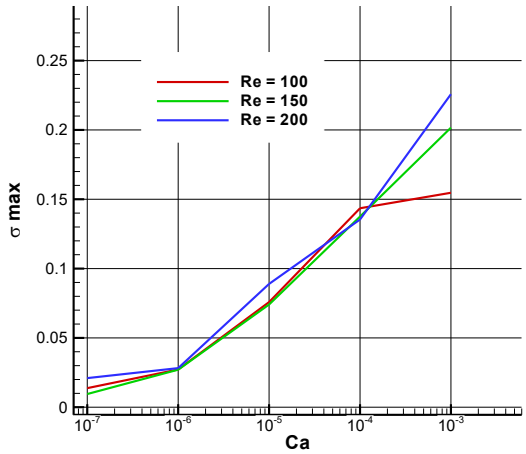

Fig. 20. Variation in elastic top wall deformation as a function of Cauchy number, for different Reynolds number at $Ha = 0$, $\varphi = 5$ %, $\gamma = 0°$ and $Pr = 10$

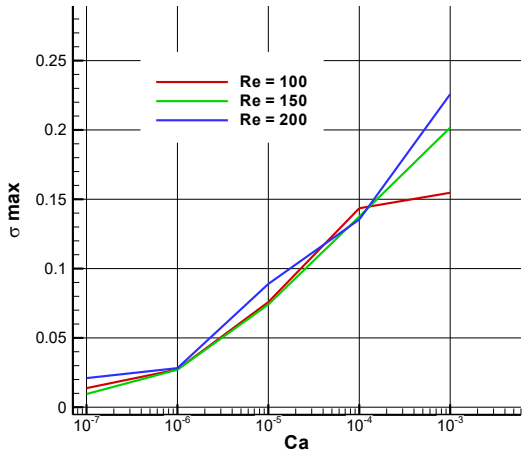

Fig. 21. Variation in elastic top wall deformation as a function of Cauchy number, for different Hartmann number at $Re = 150$, $\gamma = 0°$, $\varphi = 5$ %

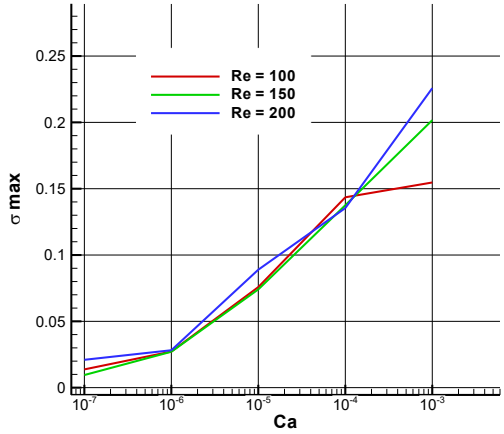

Fig. 22. Variation of elastic top wall deformation as a function of magnetic field inclination angle for various values of Hartmann number at $Re = 150$, $\varphi = 8$ %, $Ca = 10^{-4}$ and $Pr = 6.2$

Figure 22 shows the variation in elastic top wall deformation as a function of magnetic field inclination angle, for various values of Hartmann number (Ha), with defined parameters such as Re = 150, φ = 8 %, Ca = 10^{-4} and Pr = 6.2. It should be noted that increasing Ha and γ parameters influence elastic wall deformation positively. Specifically, maximum deformation is observed at an angle of inclination of 60 % degrees and a Hartmann number of 50.

Conclusions

We have conducted a numerical investigation of forced convective laminar flow over a two-dimensional downward step, involving an elastic upper wall interacting with a stationary cylinder of fixed diameter. To unravel this complex phenomenon, we employed the Galerkin finite element method, enhanced by a multigrid technique, and explored a wide range of parameters. Our findings, when compared to previous studies, provide novel insights into these fluid-structure interactions.

An increase in the Reynolds number and a decrease in the Cauchy number intensify vortex formation and disrupt the thermal boundary layer, thereby enhancing forced convective heat transfer. An increase in the Hartmann number decelerates the flow and stabilizes the thermal boundary layer, while a magnetic field inclination angle of 60° intensifies the deformation of the elastic wall and improves forced convective heat transfer.

Increasing the magnetic field inclination angle and the concentration of nanoparticles enhances heat transfer, as evidenced by an increase in the average Nusselt number, promoting convection and fluid thermal conductivity.

A decrease in the local Nusselt number is attributed to the intensification of Lorentz forces, which inhibit fluid flow and stabilize the thermal boundary layer, whereas an increase in the magnetic field inclination and nanoparticle concentration stimulates fluid motion and improves heat transfer.

CRediT authorship contribution statement

Hanaa Derraz: writing – review & editing, writing – original draft; **Mohamed Bouzit**: supervision; **Atika Bencherif**: data curation.

Conflict of interest

The authors declare that they have no conflict of interest.

References

1. Hussain S, Öztop HF. Impact of inclined magnetic field and power law fluid on double diffusive mixed convection in lid-driven curvilinear cavity. *International Communications in Heat and Mass Transfer.* 2021;127(11): 105549.
2. Kherbeet ASh, Mohammed HA, Munisamy KM, Salman BH. The effect of step height of microscale backward-facing step on mixed convection nanofluid flow and heat transfer characteristics. *International Journal of Heat and Mass Transfer.* 2014;68: 554–566.
3. Mobadersani F, Rezavand Hesari A .Magneto Hydrodynamic Effect on Nanofluid Flow and Heat Transfer in Backward-Facing Step Using Two-Phase Model. *AUT Journal of Mechanical Engineering.* 2020;4(1): 51–66.
4. Al-Aswadi AA, Mohammed H, AShuaib NH, Campo A. Laminar forced convection flow over a backward-facing step using nanofluids. *International Communications in Heat and Mass Transfer.* 2010;37(8): 950–957.

5. Turkyilmazoglu M. Nanofluid flow and heat transfer due to a rotating disk. *Computers & Fluids.* 2014;94: 139–146.
6. Selimefendigil F, Öztop HF. Identification of forced convection in pulsating flow at a backward facing step with a stationary cylinder subjected to nanofluid. *International Communications in Heat and Mass Transfer.* 2013;45: 111–121.
7. Moosavi R, Moltafet R, Lin CX, Chuang PYA. Numerical modeling of fractional viscoelastic non-Newtonian fluids over a backward facing step – Buoyancy driven flow and heat transfer. *Thermal Science and Engineering Progress.* 2021;21: 100767.
8. Hussain S, Ahmed SE. Unsteady MHD forced convection over a backward facing step including a rotating cylinder utilizing Fe_3O_4-water ferrofluid. *Journal of Magnetism and Magnetic Materials.* 2019;484: 356–366.
9. Toumi M, Bouzit M, Bouzit F, Mokhefi A. MHD forced convection using ferrofluid over a backward facing step containing a finned cylinder. *Acta Mechanica et Automatica.* 2022;16(1): 70–81.
10. Kumar S, Vengadesan S. The effect of fin oscillation in heat transfer enhancement in separated flow over a backward facing step. *International Journal of Heat and Mass Transfer.* 2019;128: 954–963.
11. Nie JH , Chen YT, Hsieh HT. Effects of a baffle on separated convection flow adjacent to backward-facing step. *International Journal of Thermal Sciences.* 2009;48(3): 618–625.
12. Lan H, Armaly BF, Drallmeier JA. Three-dimensional simulation of turbulent forced convection in a duct with backward-facing step. *International Journal of Heat and Mass Transfer.* 2009;52(7–8): 1690–1700.
13. Erturk E. Numerical solutions of 2-D steady incompressible flow over a backward-facing step, Part I: High Reynolds number solutions. *Computers & Fluids.* 2008;37(6): 633–655.
14. Mohammed HA, Fathinia F, Vuthaluru HB, Liu S. CFD-based investigations on the effects of blockage shapes on transient mixed convective nanofluid flow over a backward facing step. *Powder Technology.* 2019;346: 441–451.
15. Abu-Nada E. Application of nanofluids for heat transfer enhancement of separated flows encountered in a backward facing step. *International Journal of Heat and Fluid Flow.* 2008;29(1): 242–249.
16. Kherbeet ASh, Mohammed HA, Salman BH. The effect of nanofluids flow on mixed convection heat transfer over microscale backward-facing step. *International Journal of Heat and Mass Transfer.* 2012;55(21–22): 5870–5881.
17. Nath R, Krishnan M. Numerical study of double-diffusive mixed convection in a backward-facing step channel filled with Cu-water nanofluid. *International Journal of Mechanical Sciences.* 2019;153–154: 48–63.
18. Lv J, Hu C, Bai M, Li L, Shi L, Gao D. Visualization of SiO_2-water nanofluid flow characteristics in backward-facing step using PIV. *Experimental Thermal and Fluid Science.* 2019;101: 151–159.
19. Xie WA, Xi GN, Zhong MB. Effect of the vortical structure on heat transfer in the transitional flow over a backward-facing step. *International Journal of Refrigeration.* 2017;74: 465–474.
20. Hilo A K, Iborra A A, Sultan M T H and Hamid M F A. Experimental study of nanofluids flow and heat transfer over a backward-facing step channel. *Powder Technology.* 2020;372: 497–505.
21. Selimefendigil F, Öztop HF. Influence of inclination angle of magnetic field on mixed convection of nanofluid flow over a backward facing step and entropy generation. *Advanced Powder Technology.* 2015;26(6): 1663–1675.
22. Hussain S, Ahmed SE, Akbar T. Entropy generation analysis in MHD mixed convection of hybrid nanofluid in an open cavity with a hori zontal channel containing an adiabatic obstacle. *International Journal of Heat and Mass Transfer.* 2017;114: 1054–1066.
23. Yagoub M, Saeed Z H. Thermophysical characteristics and forced convective heat transfer of ternary doped magnetic nanofluids in a circular tube: An experimental study. *Case Studies in Thermal Engineering.* 2023;52: 103748.
24. Yoon HS, Seo JH, Kim JH. Laminar forced convection heat transfer around two rotating side-by-side circular cylinder. *International Journal of Heat and Mass Transfer.* 2010;53(21–22): 4525–4535.
25. Sarkar S, Ganguly S, Biswas G, Saha P. Effect of cylinder rotation during mixed convective flow of nanofluids past a circular cylinder. *Computers & Fluids.* 2016;127: 47–64.
26. Xie WA, Xi GN. Flow instability and heat transfer enhancement of unsteady convection in a step channel. *Alexandria Engineering Journal.* 2022;61(9): 7377–7391.
27. Toumi M, Bouzit M, Mokhefi A, Derbal D. Unsteady numerical investigation of ferrofluid forced convection over a downward step containing a rotating finned cylinder. *Journal of the Serbian Society for Computational Mechanics.* 2022;16(2): 67–86.
28. Hussein AK, Bakier MA, Ben Hamida MB, Sivasankaran S. Magneto hydrodynamic natural convection in an inclined T-shaped enclosure for different nanofluids and subjected to a uniform heat source. *Alexandria Engineering Journal.* 2016;55(3): 2157–2169.
29. Selimefendigil F, Öztop HF. Effect of a rotating cylinder in forced convection of ferrofluid over a backward facing step. *International Journal of Heat and Mass Transfer.* 2014;71: 142–148.

30. Geridönmez BP, Öztop HF. Effects of inlet velocity profiles of hybrid nanofluid flow on mixed convection through a backward facing step channel under partial magnetic field. *Chemical Physics.* 2021;540: 111010.
31. Sheikholeslamia M , Hayatb T, Alsaedi A. Numerical simulation for forced convection flow of MHD CuO-H2O nanofluid inside a cavity by means of LBM. *Journal of Molecular Liquids.* 2018;249: 941–948.
32. Selimefendigil F, Öztop HF. Forced convection of nanofluid in double vented cavity system separated by perforated conductive plate under magnetic field. *Engineering Analysis with Boundary Elements.* 2023;149: 18–26.
33. Al-Amir QR, Hamzah HK, Ali FH, Bayraktar S, Arici M, Hatami M. Comparison study of vertical and horizontal elastic wall on vented square enclosure filled by nanofluid and hexagonal shape with MHD effect. *The European Physical Journal Special Topics.* 2022;231: 2623–2643.
34. Selimefendigil F, Öztop HF, Abu-Hamdeh N. Impacts of conductive inner L shaped obstacle and elastic bottom wall on MHD forced convection of a nanofluid in vented cavity. *Journal of Thermal Analysis and Calorimetry.* 2020;141: 465–482.
35. Sheikholeslami M, Keramati H, Shafeed A, Li Zh, Alawad OA, Tlili I. Nanofluid MHD forced convection heat transfer around the elliptic obstacle inside a permeable lid drive 3D enclosure considering lattice Boltzmann method. *Physica A: Statistical Mechanics and its Applications.* 2019;523; 87–104.
36. Ahmed Sh, Hossain A, Zahangir Hossain Md, Mamun Molla Md. Forced convection of non-Newtonian nanofluid in a sinusoidal wavy channel with response surface analysis and sensitivity test. *Results in Engineering.* 2023;19: 101360.
37. Derikvand M, Solari MSh, Toghraie D. Entropy generation and forced convection analysis of ethylene glycol/MWCNTs-Fe_3O_4 non-Newtonian nanofluid in a wavy microchannel with hydrophobic surfaces. *Journal of the Taiwan Institute of Chemical Engineers.* 2023;143: 104707.
38. Ghasemi K, Siavashi M. Three-dimensional analysis of magnetohydrodynamic transverse mixed convection of nanofluid inside a lid-driven enclosure using MRT-LBM. *International Journal of Mechanical Sciences.* 2022;165: 105199.
39. Jamshed W, Eid MR, Hussain SM, Abderrahmane A, Safdar R, Younis O, Pasha AA. Physical specifications of MHD mixed convective of Ostwald-de Waele nanofluids in a vented-cavity with inner elliptic cylinder. *International Communications in Heat and Mass Transfer.* 2022;134: 106038.
40. Hamzah HK, Al-Amir QR, Abdulkadhim A, Ahmed SY, Ali FH, Abed AM, Abed IM. In a Vented Square Enclosure, the Effect of a Flexible Baffle Attached to a Solid Cylinder on Mixed Convection. *Arabian Journal for Science and Engineering.* 2022;47: 15489–15504.
41. Derraz H, Bouzit M, Mokhfi A, Bencherif A, Toumi M. Numerical study of natural convection of Bingham fluid using a flexible fin. *International Journal of Thermofluid Science and Technology.* 2024;11(2): 110202.

Appendix A. Nomenclature

B_0	Magnetic field strength, Tesla
D_s	dimensionless displacement vector
H	heat transfer coefficient, W/m^2 K
Ha	Hartmann number, $B_0 H \sqrt{\frac{\sigma_{nf}}{\mu_{nf}}}$
K	thermal conductivity, W/m K
H	inlet step height, m
n	normal coordinate
Nu	Local Nusselt number
Nu_{avg}	averaged Nusselt number
p	pressure, Pa
P	non-dimensional pressure
Pr	Prandtl number, $\frac{\nu_f}{\alpha_f}$
Re	Reynolds number, $\frac{H\bar{u}}{\nu_f}$
T	temperature, K
c_p	thermal specific heat, J/Kg K
Ca	Cauchy number
u, v	x−y velocity components, m/s
U, V	dimensionless velocity components
x, y	Cartesian coordinates, m
X, Y	dimensionless coordinates
t	time
$\bar{u}$	average velocity, m s^{-1}

Greek symbols

ϕ	nanoparticle concentration
α	thermal diffusivity, m^2/s
β	expansion coefficient, 1/K
γ	inclination angle of magnetic field
θ	dimensionless temperature, $\frac{T-T_c}{T_h-T_c}$
ν	kinematic viscosity, m2/s
ρ	density of the fluid, kg/m^3
σ^*	the solid stress tensor
μ	dynamic viscosity, N s/m^2
τ	dimensionless time

Subscripts

c	cold
h	hot
avg	average
nf	nanofluid
f	fluid
s	solid